

Statistical distribution of gravitational-lensing excursion angles: Winding ways to us from the deep universe

Takashi Hamana¹, Matthias Bartelmann², Naoki Yoshida³, Christoph Pfrommer⁴

¹ National Astronomical Observatory of Japan, Mitaka, Tokyo 181-8588, Japan

² ITA, Universität Heidelberg, Tiergartenstr. 15, D-69121 Heidelberg, Germany

³ Department of Physics and Astrophysics, Nagoya University, Nagoya 464-8602, Japan

⁴ Max-Planck-Institut für Astrophysik, Karl-Schwarzschild-Strasse 1, D-85748 Garching, Germany

Accepted *****; Received *****; in original form 2004 July 29

ABSTRACT

We investigate statistical distributions of differences in gravitational-lensing deflections between two light rays, the so-called lensing excursion angles. A probability distribution function of the lensing excursion angles, which plays a key role in estimates of lensing effects on angular clustering of objects (such as galaxies, QSOs and also the cosmic microwave background temperature map), is known to consist of two components; a Gaussian core and an exponential tail. We use numerical gravitational-lensing experiments in a Λ CDM cosmology for quantifying these two components. We especially focus on the physical processes responsible for generating those two components. We develop a simple empirical model for the exponential tail which allows us to explore its origin. We find that the tail is generated by the coherent lensing scatter by massive halos with $M > 10^{14}h^{-1}M_\odot$ at $z < 1$ and that its exponential shape arises due to the exponential cut-off of the halo mass function at that mass range. On scales larger than 1 arc minute, the tail does not have a practical influence on the lensing effects on the angular clustering. Our model predicts that the coherent scatter may have non-negligible effects on angular clustering at sub-arcminute scales.

Key words: gravitational lensing – cosmology: theory – dark matter – large-scale structure of universe

1 INTRODUCTION

Light rays are deflected when they propagate through an inhomogeneous gravitational field, such as the real universe we live in. The lensing deflection angle varies from one direction to another, and thus the difference in deflection angles between two light rays, which we call the “lensing excursion angle”, does as well. Consequently, it is not easy to infer the transverse distance between two celestial objects at a cosmological distance from their angular separation in the sky. Strictly speaking, lacking complete knowledge of the matter distribution in the universe, this is impossible to do.

Since distance is one of most fundamental physical quantities, the lack of a precise distance measure to the far universe may prevent us from a detailed understanding of the universe. A well known case is that angular correlations of distant galaxies and of the temperature map of the cosmic microwave background are altered by lensing deflections (see §9 of Bartelmann & Schneider 2001 for a review and references therein).

Although we cannot know the lensing excursion angle for an individual pair of light rays, knowledge of their statistical distribution greatly helps us in estimating the order

of magnitude of lensing effects. In addition, it allows the intrinsic angular correlation functions to be deconvolved from measured correlation functions (Bartelmann & Schneider 2001). It is thus of fundamental importance to understand in detail the statistical distribution of the lensing excursion angles.

The analytic model for computing the variance of lensing excursion angles in a framework of modern cosmological models was developed by Seljak (1994; 1996), based on the linear perturbation theory (the so-called power spectrum approach). Hamana & Mellier (2001) performed numerical experiments of the gravitational lensing deflections in cold dark matter models and examined the statistical properties of the lensing excursion angles. They found that the probability distribution function (PDF) of the excursion angles consists of two components, a Gaussian core and an exponential tail, and that the variance of the Gaussian core component agrees well with the prediction by the power spectrum approach. They argued that the exponential tail may be generated by coherent lensing scattering by massive halos which is not taken into account in the power spectrum approach.

The purpose of this paper is twofold: The first is to explore the origin of the exponential tail of the lensing excursion angle PDF. The second is to develop an empirical model for the exponential tail. To pursue these purposes, we first examine in detail properties of the exponential tail of the excursion-angle PDF using numerical experiments in §2. Then in §3, we describe a model for the exponential tail which is based on the assumption that the tail originates from coherent lensing scattering by individual massive dark-matter halos, and compare the model predictions with numerical results. We also discuss a general picture of the light propagation in the universe paying special attention to the role of secular random deflections by either large or small-scale structures and a coherent scatter by a massive halo. Finally, we give a summary and discussion in §4.

2 RAY-TRACING SIMULATION

2.1 VLS *N*-body simulation

We performed weak lensing ray-tracing experiments in a Very Large *N*-body Simulation (VLS) carried out by the Virgo Consortium (Jenkins et al. 2001, and see also Yoshida, Sheth & Diaferio 2001 for simulation details). The simulation was carried out using a parallel P³M code (MacFarland et al. 1998) with a force softening length of $l_{\text{soft}} \sim 30 h^{-1} \text{kpc}$. The simulation employed 512^3 CDM particles in a cubic box of $479 h^{-1} \text{Mpc}$ side length, which gives a particle mass of $m_{\text{part}} = 6.86 \times 10^{10} h^{-1} M_{\odot}$. It uses a flat cosmological model with a matter density $\Omega_0 = 0.3$, a cosmological constant $\Omega_{\Lambda} = 0.7$, and a Hubble constant $H_0 = 100h$ with $h = 0.7$. The initial matter power spectrum was computed using CMBFAST (Seljak & Zaldarriaga 1996) assuming a baryonic matter density of $\Omega_b = 0.04$. The normalization of the power spectrum is taken as $\sigma_8 = 0.9$.

2.2 Weak lensing ray-tracing simulation

The multiple-lens plane ray-tracing algorithm we used is detailed in Hamana & Mellier (2001; see also Bartelmann & Schneider 1992 and Jain, Seljak & White 2000; Hamana, Martel, Futamase 2000; Vale & White 2003 and Hamana, Takada & Yoshida 2004 for the theoretical basics and technical issues); thus in the following we describe only aspects specific to the VLS simulation data and to ray-tracing experiments in this study.

We use thirteen snapshot outputs from two runs of the *N*-body simulation which differ only in the realization of the initial fluctuation field. A stack of these outputs provides the density field from $z = 0$ to $z = 6.8$. We do not use further higher redshift outputs because of two reasons; (1) discreteness effects of particles (Hamana, Yoshida & Suto 2002), and (2) an artificial power excess in the density power spectrum due to the “glass” initial condition (White 1996) at around the mean separation length of particles, both of them are significant at such high redshifts. For higher redshifts up to the last scattering surface ($z \approx 1100$), we simply consider a homogeneous density field. Thus within $6.8 < z < 1100$ rays propagate as in a perfectly homogeneous universe. This treatment misses lensing contributions from structures at

that redshift range. It has turned out that this approximation causes only a minor effect. We will discuss its influences on our analyses later.

Each *N*-body box is divided into 4 sub-boxes with an equal thickness of $119.75 h^{-1} \text{Mpc}$. The *N*-body particles in each sub-box are projected onto *lens planes*. In this way, the particle distribution between an observer and $z = 6.8$ is projected onto 50 lens planes. Note that, in order to minimize the difference in redshift between a lens plane and an output of *N*-body data, only one half of the data (i.e. two sub-boxes) of $z = 0$ output is used. The particle distribution on each plane is converted into the surface density field on a 2048^2 regular grid using the triangular shaped cloud (TSC) assignment scheme (Hockney & Eastwood 1988). The grid size is $0.23 h^{-1} \text{Mpc}$ which is chosen to maintain the resolution provided by the *N*-body simulation and removing at the same time the shot noise due to discreteness in the *N*-body simulation (this choice is equivalent to the “large-scale smoothing” in Ménard et al., 2003, we refer the reader to this reference for further examination of the effective resolution of the ray-tracing simulation). Its computation follows the procedure described in Hamana & Mellier (2001).

Having produced surface density fields on all lens planes, 1024^2 rays are traced backwards from the observer’s point using the multiple-lens plane algorithm (e.g. Schneider, Ehlers & Falco 1992). The initial ray directions are set on 1024^2 grids with a grid size of 0.25 arcmin , thus the total area covered by rays is $4.27^2 \text{ square degrees}$. We produced 36 realizations of the underlying density field by randomly shifting the simulation boxes in the direction perpendicular to the line-of-sight using the periodic boundary conditions of the *N*-body boxes.

The 36 realizations are not perfectly independent because they are generated from the same *N*-body outputs (but using different combinations of random lines of sight) which come from two runs of *N*-body simulation. Therefore the generated lensing data (the lensing deflection field, lensing convergence and shear map) are subject to sample variance. In order to test its magnitude, we compare the convergence two-point correlation function with its theoretical prediction (Jain & Seljak 1997) in Figure 1. The measurements from the ray-tracing experiment are plotted by symbols with error bars which represent the mean and root-mean-square among the 36 realizations, while the solid lines show the prediction. Note that the measurement for $z_s = 1100$ should be compared with the dotted line which shows the theoretical prediction for $z_s = 1100$ but the contribution from the density fluctuations between $z = 6.8$ and 1100 is ignored. The measurements are in good agreement with the theoretical prediction in shape, but are slightly higher in amplitude. This excess may be mostly attribute to the sample variance and implies that there exists an excess power in the lensing potential field. Since lensing deflections result from the same potential field, it is expected that there exists, to a similar extent, an excess in the deflection angle statistics. On scales smaller than 1 arcmin, the slope of the measured correlation function becomes flatter than predicted; this is due to the limited resolution of the *N*-body simulation. The effective angular resolution of the convergence field is about 1 arcmin for lower redshift ($z_s < 3$) and is slightly better for higher redshifts (see Ménard et al., 2003 for further discussion on the resolution issue).

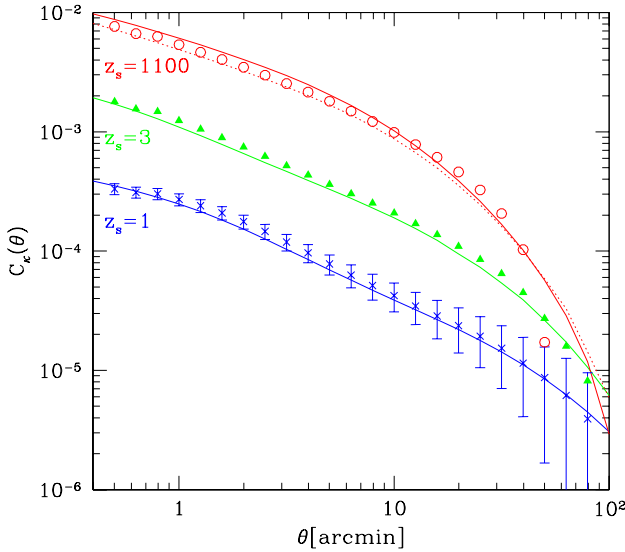


Figure 1. The convergence two-point correlation functions. Measurements from ray-tracing experiments are shown by symbols with error bars which represent the mean and root-mean-square among the 36 realizations. Crosses, filled triangles and open circle are for $z_s = 1$, 3 and 1100, respectively. The error bars of the cases for $z_s = 3$ and 1100 are not displayed for clarity but are as similar magnitude as the $z_s = 1$ case. The solid lines show the theoretical prediction (e.g., Jain & Seljak 1997) in which the fitting function of nonlinear power spectrum by Peacock & Dodds (1996) is used to include the effect of the nonlinear growth of the density field. The dotted line shows the theoretical prediction for $z_s = 1100$ but the contribution from density fluctuation at $6.8 < z < 1100$ is not integrated.

2.3 PDF of the lensing excursion angles

Using weak-lensing experiments, we study the statistics of differences in deflection angles between two light rays, which we refer to as the ‘‘lensing excursion angle’’. The deflection angle of a light ray, which is computed by the lens equation, is simply the difference between its positions θ_I and θ_S on the image and source planes, respectively. Denoting the deflection angle of two rays by α^1 and α^2 , respectively, we write the lensing excursion angle between these rays as $\delta\alpha = \alpha^1 - \alpha^2$. Similarly we denote their intrinsic separation by $\theta_{12} = |\theta_S^1 - \theta_S^2|$.

Let us first look into the probability distribution function (PDF) of the lensing excursion angles which is one of most fundamental statistics. Figure 2 shows the PDFs of the lensing excursion angles normalized by its intrinsic separation (i.e. $\delta\alpha/\theta_{12}$). Since the vector field $\delta\alpha$ has no preferred direction, we use both components, $\delta\alpha_1$ and $\delta\alpha_2$, to compute the PDFs. The dotted lines in each plot of Figure 2 show the Gaussian PDF with its standard dispersion (σ^2) computed from the PDF itself (i.e. $\sigma^2 = \int dx x^2 \text{PDF}(x)$). As was first pointed out by Hamana & Mellier (2001), the PDFs consist of two components, a Gaussian core and the exponential tail, which are generated by different physical processes as we will discuss below.

The origin of the Gaussian core is explained as follows: Light rays from a cosmological distance undergo many (either strong or weak) gravitational lensing deflections. Since the spatial distribution of lenses at a large separation are un-

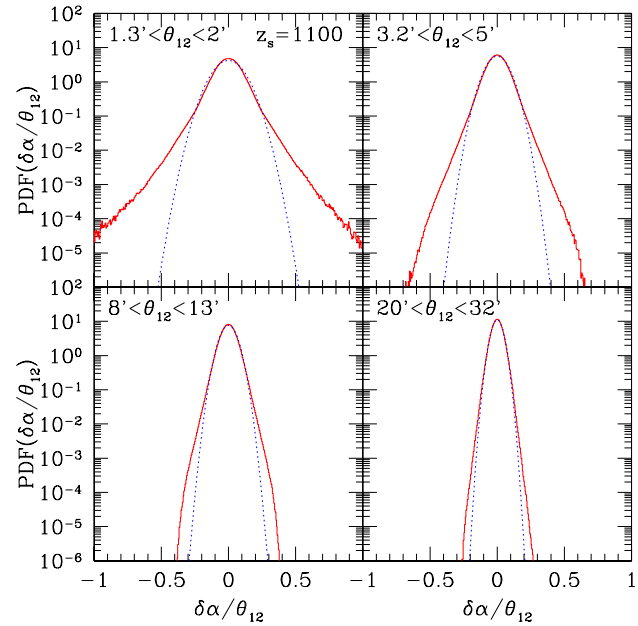


Figure 2. The solid curves show the probability distribution function of the lensing excursion angles normalized by the intrinsic ray separation. The source redshift is $z_s = 1100$. The ranges of the intrinsic separation of the light-ray pairs θ_{12} are given in each panel. The dotted curves show Gaussian distributions with their σ computed from the measured PDFs (i.e., $\sigma^2 = \int dx x^2 \text{PDF}(x)$).

correlated, rays basically undergo many uncorrelated deflections. Provided the separation between two rays is so large that effects of coherent scattering can be ignored, two light rays undergo independent deflections. According to the central limit theorem, the statistical distribution of the lensing excursion angles of such light-ray pairs is given by a Gaussian. A necessary condition for the central limit theorem to hold is that the parent distribution of the individual events which are being superposed has finite variance. The deflection angle calculated in the weak-lensing regime using the power-spectrum approach has finite variance (Seljak 1994; 1996), but it is based on linearized gravity and ignores lensing by individual halos. On the other hand, numerical gravitational lensing experiments show that the PDF consists of the Gaussian core and the exponential tail. In order to understand whether the Gaussian core can indeed be caused by the superposition of many deflections, we need to investigate the variance of the excursion angle. In particular, the numerical experiments miss the influence of numerous distant lenses, because of their necessarily finite volume. We will now show, using a simple approach, that accumulated contributions from very distant lenses do not significantly affect the excursion angle variance, thus it remains finite.

Consider first a single light ray passing the lens plane in the origin. There is a finite number of lenses close to the ray, thus we can restrict ourselves to distant lenses since we are investigating whether the deflection-angle variance is finite or not. Axially symmetric lenses more distant than their (e.g. virial) radii act as point lenses, thus we can approximate their deflection angles by $\vec{\alpha}_i = \vec{\theta}_i/\theta_i^2$. Assuming the lenses have a number density n and are randomly distributed, the variance of the total deflection angle con-

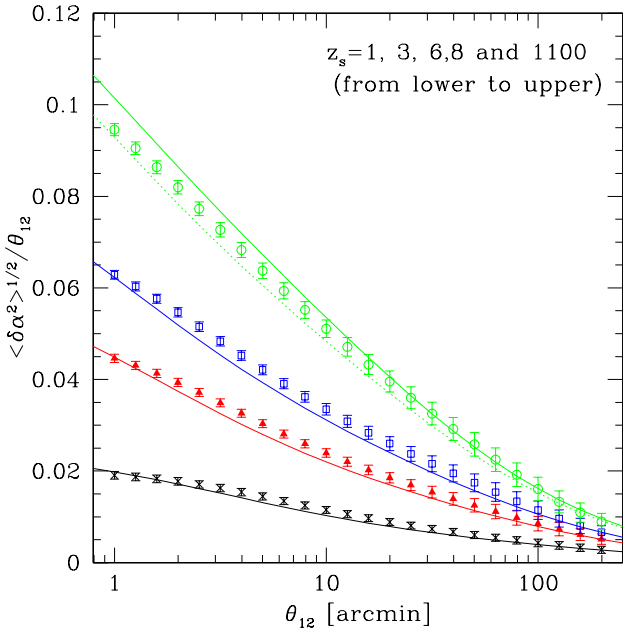


Figure 3. The standard dispersion of the lensing excursion angles plotted as the function of the separation angle. Symbols and error bars show the mean and RMS among 36 realizations of the ray-tracing numerical experiments. Solid lines represent the theoretical predictions from the power spectrum approach (Seljak 1996), in which the fitting function of the nonlinear power spectrum by Peacock & Dodds (1996) was used. The source redshifts are, from lower to higher, $z_s=1, 3, 6.8$ and 1100 , respectively. The dotted line shows the theoretical prediction for $z_s = 1100$ but the contribution from density fluctuation at $6.8 < z < 1100$ is ignored.

tributed by lenses in a ring around the origin with radius θ and width $d\theta$ is

$$\langle \vec{\alpha}^2 \rangle = \left\langle \sum_{i=1}^N \frac{1}{\theta^2} \right\rangle = \frac{2\pi n\theta d\theta}{\theta^2} = 2\pi n d \ln \theta. \quad (1)$$

Integrating over θ shows that the variance diverges logarithmically.

The situation changes for the excursion angle. Consider two light rays piercing the lens plane at positions $\vec{\theta}_{1,2} = (\mp d/2, 0)$. Specializing again to distant lenses, we can approximate the individual deflection angles by those of point lenses. The excursion angle of the lenses in a ring of radius θ and width $d\theta$ around the origin can then be expanded to lowest order in d/θ ,

$$\delta\vec{\alpha}(\theta) = \sum_{i=1}^N \frac{d}{\theta^2} (-\cos 2\phi_i, \sin 2\phi_i), \quad (2)$$

where ϕ_i is the polar angle of the i -th lens. Again assuming randomly distributed lenses, the variance of the excursion angle contributed by the lenses in the ring is thus

$$\langle \delta\vec{\alpha}^2(\theta) \rangle = \left\langle \sum_{i=1}^N \frac{\pi d^2}{\theta^4} \right\rangle = \frac{2\pi^2 d^2 n \theta d\theta}{\theta^4}, \quad (3)$$

i.e. the excursion-angle variance converges like θ^{-2} when integrated over θ to infinity. Thus, we can apply the central

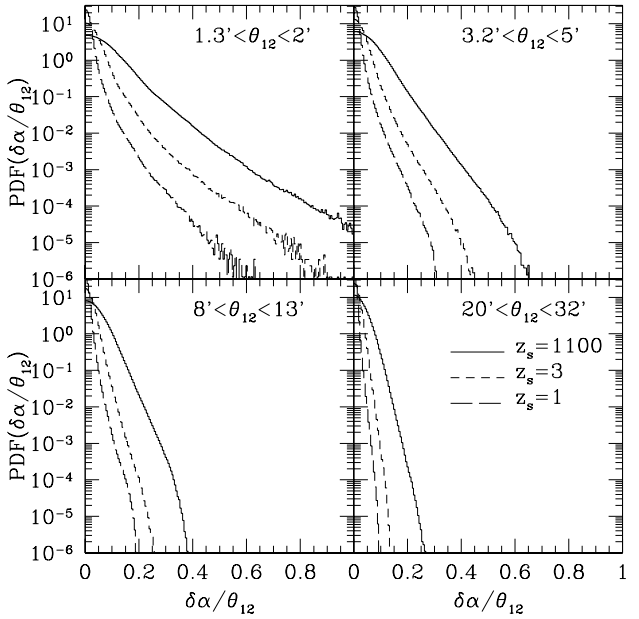


Figure 4. The PDF of lensing excursion angles normalized by its intrinsic separation (plotted positive side only). The source redshifts are, from narrower to broader PDF, $z_s=1, 3$ and 1100 , respectively. As these plots show, for a given θ range, the amplitude of the PDF tail becomes higher as z_s increases, while their slope is almost unchanged for plotted redshifts $z_s > 1$.

limit theorem to the excursion angle, while we could not for the deflection angle itself.

Now we test the theoretical model prediction for the variance of the excursion angles developed by Seljak (1994; 1996) against our numerical results. Figure 3 compares the standard dispersion measured from the numerical experiments with the theoretical prediction. The dispersion becomes larger as the light rays travel a longer distance, because the rays can undergo more deflections. It is found in the plot that the measurements are slightly larger than the prediction. However, a similar excess is seen in the convergence correlation function (Figure 1), thus this is mostly due to the sample variance. We may therefore conclude that the power spectrum approach provides a good prediction even for $z_s = 1100$, and the non-Gaussian tail has no strong contribution to the variance. It is important to notice that coherent scattering by lensing due to massive halos that generate the exponential tail contribute only very little to the excess in the measured dispersion over the prediction.

Let us now turn to the tail of the lensing excursion angle PDF. Figure 4 compares the PDF obtained from the ray-tracing numerical experiments for three source redshifts, $z_s = 1, 3$ and 1100 , and for various ranges of ray separations. This Figure represents major characteristics of the non-Gaussian tail: (a) it has an approximately exponential slope; (b) it changes little with the source redshift, but its amplitude increases with the source redshift, at least within the redshift range we consider ($z_s > 1$). We fit the tail of the PDFs to the exponential distribution:

$$E(x) = p \exp(-qx). \quad (4)$$

To do this, we take two points x_1 and x_2 such that $\text{PDF}(x_1) = 1.0 \times 10^{-2}$ and $\text{PDF}(x_2) = 1.0 \times 10^{-3}$. The

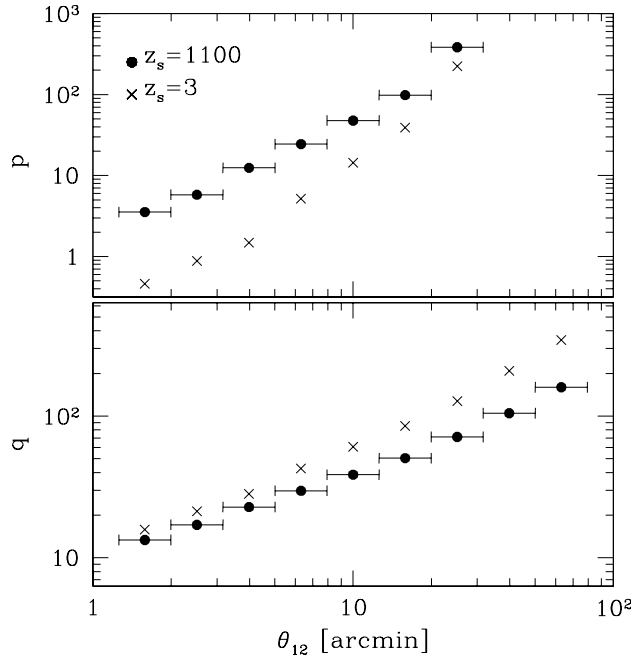


Figure 5. Parameters in the exponential distribution (eq. 4) computed by fitting to the non-Gaussian tail of PDFs from ray-tracing experiments. The filled circles and crosses show the results from the $z_s = 1100$ and $z_s = 3$ cases, respectively. The error bars represent the ranges of ray separations taken to compute the PDFs.

comparison between the results of $z_s = 3$ and $z_s = 1100$ plotted in Figure 5 confirms the above point (b) in a quantitative manner. Note that fitting the exponential function to the PDF tails becomes poor for large ray separations because the non-Gaussian tail does not appear prominently due to the limited statistics. This accounts for the steep rise of both p and q at large θ_{12} which rather reflects the slope of the Gaussian core.

In the next section, we develop a model of the exponential tail and explore its origin. To do this, a visual impression from Figure 6 could be informative. In this figure, the celestial distributions of ray pairs having a large lensing excursion angle and of massive halos in one realization of the numerical experiment are displayed (see Hamana et al. 2004 for a detailed description of the construction of a halo catalog on a light-cone). Only the halos within the redshift interval between 0 and 1 are plotted using black symbols. Red dots represent the ray pairs which obey the following criteria, an unlensed ray separation of $\theta_{12} > 1$ arcmin and an excursion angle of $|\delta\alpha|/\theta_{12} > 0.7$. Apparently, most of large excursion angle ray pairs pass very close to a massive halo. We argue in the following section that the exponential tail results from coherent strong deflections of two nearby rays by a massive halo, and explain the origin of the above characteristics using simple models.

3 ORIGIN OF THE EXPONENTIAL TAIL OF THE EXCURSION ANGLE PDF

In this section we explore the origin of the exponential tail of the excursion angle PDF found in the ray-tracing numerical experiments. For this purpose, we focus on the tail

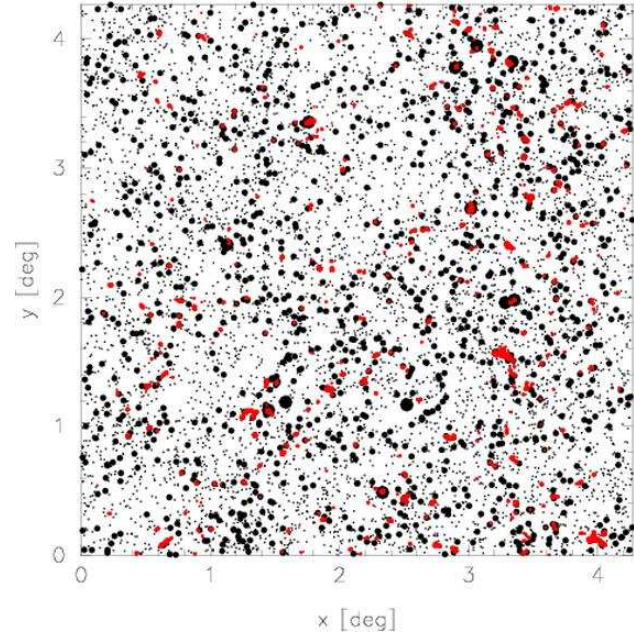


Figure 6. The celestial distributions of ray pairs having a large lensing excursion angle and of massive halos in one realization of the numerical experiment. See Hamana et al. (2004) for a detailed description of construction of the halo catalog on a light-cone. Black symbols represent halos; the large filled circles, small filled circles and dots are for halos with $M_{\text{halo}} > 4 \times 10^{14}$, $4 \times 10^{14} > M_{\text{halo}} > 4 \times 10^{13}$ and $4 \times 10^{13} > M_{\text{halo}} > 1 \times 10^{13}$ [$h^{-1} M_{\odot}$], respectively. Only the halos within the redshift interval between 0 and 1 are displayed. Red dots represent the ray pairs which obey the following criteria, an unlensed ray separation of $\theta_{12} > 1$ arcmin and an excursion angle of $|\delta\alpha|/\theta_{12} > 0.7$. The middle points of ray pairs are displayed.

part and do not consider the Gaussian core whose origin has been investigated in the literature (Seljak 1994; 1996; see also chapter 9 of Bartelmann & Schneider) and also in the last section. We develop a theoretical model from two assumptions: Large excursion angles are mainly caused by the strong lensing of a massive halo, and the probability for a ray to undergo multiple strong lensing events is negligible. The former is reasonable because a process that is not taken into account in the power spectrum approach could generate non-Gaussian features. Also the visual impression from Figure 6 could be a support of that idea. The latter is validated by the observational fact of the small cross section for strong lensing events by a single lens (either a galaxy or cluster of galaxies) such as multiply-imaged QSOs and strongly-lensed arc-like images of distant galaxies. Thus, it is certain that multiple scattering by more than one massive halo is very rare.

We consider the same Λ CDM cosmology as one adopted for the numerical experiments in §2. We denote the PDF for finding a ray pair with θ_{12} having the excursion angle $\delta\alpha$ by $\text{PDF}(\delta\alpha|\theta_{12})$.

3.1 Lensing deflection by a universal density profile halo

Navarro Frenk & White (1996; 1997, NFW hereafter) found from N -body simulations that the density profile of dark

matter halos can be fitted by a universal form regardless of their mass and redshift. We adopt a truncated universal profile;

$$\rho(x) = \frac{\rho_s}{x^s(1+x)^{3-s}}, \quad x = \frac{r}{r_s}, \quad (5)$$

for $r < r_{\text{vir}}$ and 0 otherwise, where r_s and r_{vir} are the scale radius and virial radius, respectively. It is convenient to introduce the concentration parameter $c_{\text{vir}} = r_{\text{vir}}/r_s$. Navarro et al. (1996) proposed the universal inner slope of $s = 1$, while a steeper slope was claimed by later studies using higher resolution N -body simulations; Moore et al. (1998; 1999), Ghigna et al. (2000) and Fukushige & Makino (2001; 2003) found larger values such as $s = 1.5$, while Jing (2000) and Jing & Suto (2000) pointed out that it varies from 1.1 to 1.5 and argued a possible weak dependence on the halo mass. In this paper, we consider two cases $s = 1$ and 1.5. Navarro et al. (1997) and Bullock et al. (2001) have extensively examined a relation between the concentration parameter and the halo mass and its redshift evolution adopting a fixed value of $s = 1$. We adopt a generalized mass-concentration relation proposed by Oguri, Taruya & Suto (2001; see also Keeton & Madau 2001);

$$c_{\text{vir}}(M, z) = (2-s) \frac{c_*}{1+z} \left(\frac{M}{10^{14} h^{-1} M_\odot} \right)^{-0.13}. \quad (6)$$

Bullock et al. (2001) suggested $c_* \sim 8$ for the Λ CDM model, which we adopt as a fiducial choice. We note that there is a relatively large scatter in this relation (Bullock et al. 2001; Jing 2000). The virial mass (defined by the mass within the virial radius r_{vir}) of the universal halo is given by

$$M_{\text{vir}} = 4\pi \rho_s r_{\text{vir}}^3 \frac{m(c_{\text{vir}}, s)}{c_{\text{vir}}^3}, \quad (7)$$

with

$$m(c_{\text{vir}}, s) = \int_0^{c_{\text{vir}}} dx \frac{x^{2-s}}{(1+x)^{3-s}}. \quad (8)$$

Since the spherical collapse model indicates that $M_{\text{vir}} = 4\pi r_{\text{vir}}^3 \delta_{\text{vir}}(z) \bar{\rho}_0/3$, where δ_{vir} is the over-density of collapse (see Nakamura & Suto 1997 and Henry 2000 for useful fitting functions), one can express ρ_s in terms of $\delta_{\text{vir}}(z)$, c_{vir} and s :

$$\rho_s = \frac{\delta_{\text{vir}} \bar{\rho}_0}{3} \frac{c_{\text{vir}}^3}{m(c_{\text{vir}}, s)}. \quad (9)$$

Let us summarize basic equations for gravitational lensing properties of the truncated universal profile halo (Takada & Jain 2003, see Bartelmann 1996; Wright & Brainerd 2000; Oguri et al. 2001 for lensing properties of the non-truncated universal profile lens model). The surface mass density of the truncated universal profile halo is given by,

$$\Sigma(y) = \int_{-\sqrt{c_{\text{vir}}^2 - y^2}}^{\sqrt{c_{\text{vir}}^2 - y^2}} dz \rho(y, z) = 2\rho_s r_s f(y), \quad y = \frac{r}{r_s}, \quad (10)$$

with

$$f(y) = \int_0^{\sqrt{c_{\text{vir}}^2 - y^2}} dz \frac{1}{(y^2 + z^2)^{s/2} (1 + \sqrt{y^2 + z^2})^{(3-s)}}, \quad (11)$$

for $y \leq c_{\text{vir}}$ and $f(y) = 0$ otherwise. The projected mass within a radius b is

$$\begin{aligned} M(< b) &= 2\pi \int_0^b dy' y' \Sigma(y') \\ &= 4\pi r_s^3 \rho_s \int_0^h dy y f(y), \end{aligned} \quad (12)$$

where $h = b/r_s$. We perform the above integration numerically. The thin lens equation is written by

$$\theta_S = \theta_I - \alpha(D_l \theta_I), \quad (13)$$

with

$$\alpha(b) = \frac{4GM(< b)}{c^2 b} \frac{D_{ls}}{D_s}. \quad (14)$$

In the last expression, the origin of the coordinates is taken at the lens center, $b = D_l \theta_I$ is the impact parameter, and D_l , D_{ls} and D_s are the angular diameter distances from observer to lens, from lens to source, and from observer to source, respectively. The deflection angle of the truncated universal profile halo is given by,

$$\alpha(\theta) = \alpha_* g(\theta), \quad (15)$$

with

$$g(\theta) = \frac{c_{\text{vir}}}{m(c_{\text{vir}}, s)} \frac{\int_0^x dy y f(y)}{x}, \quad x = \frac{D_l \theta}{r_s} \quad (16)$$

and

$$\begin{aligned} \alpha_* &= 2\Omega_m \frac{D_{ls}}{D_s} \left(\frac{H_0}{c} \right)^2 r_{\text{vir}}^2 \delta_{\text{vir}} \\ &\simeq 4'' \left(\frac{M_{\text{vir}}}{10^{14} h^{-1} M_\odot} \right) \left(\frac{r_{\text{vir}}}{1 h^{-1} \text{Mpc}} \right)^{-1} \frac{D_{ls}}{D_s}. \end{aligned} \quad (17)$$

Note that $\alpha_* \propto M^{2/3}$. It is important to notice that a dependence of the halo profile parameters on the deflection angle enters only through the function $g(\theta)$. Note that for $\theta \geq \theta_{\text{vir}}$ it reduces to $g(\theta) = \theta_{\text{vir}}/\theta$ (where θ_{vir} is the angular virial radius defined by $\theta_{\text{vir}} = r_{\text{vir}}/D_l$). In Figure 7, the function $g(\theta)$ is plotted for various value of c_* . As one may see in the Figure, the deflection angle profile $g(\theta)$ peaks at $\theta \sim \theta_{\text{vir}}/c_* = \theta_s$ ($\theta_s = r_s/D_l$) and the peak value does not strongly depend on the inner slope s . It is also found that the peak value relates to the concentration parameter roughly by $g_{\text{max}} \sim 0.1 c_* + 1$. Therefore, in a reasonable range of c_* the maximum deflection angle by a single universal halo lens is $\alpha_{\text{max}} = (1-3)\alpha_*$. One may also find that at the inner part, the deflection angle is larger for a larger c_* or for a steeper inner slope (thus for more centrally concentrated halos). We find that $g(\theta)$ has an asymptotic inner slope of $\propto \theta^{0.82}$ ($\propto \theta^{0.48}$) for $s = 1$ ($s = 1.5$).

3.2 Lensing excursion angles

Since the deflection angle of a universal density profile halo is finite, the excursion angle is finite as well. Clearly, the largest excursion angle is $2\alpha_{\text{max}}$ which happens when one ray passes at the distance $\sim \theta_s$ from the lens and the other ray passes at the same distance in the opposite side of the lens. Thus this happens only if $\theta_{12} = 2\theta_s$, and is very rare. Let us consider the maximum excursion angle produced for other ray separations. If $\theta_{12} > \theta_s$, the largest excursion angle

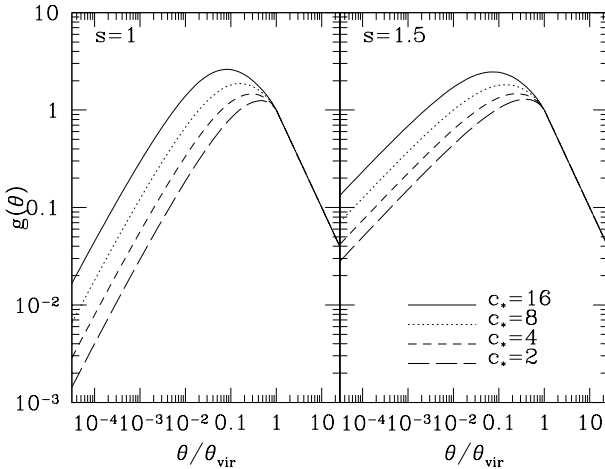


Figure 7. Deflection angle profiles of the truncated universal density profile lens, $g(\theta)$ defined in eq. (16), as a function of the impact parameter (normalized by the angular virial radius) for various concentration parameters denoted in the plot. The left panel is for $s = 1$ and right panel for $s = 1.5$. Note that $g(\theta)$ has an asymptotic inner slope of $\propto \theta^{0.82}$ ($\propto \theta^{0.48}$) for $s = 1$ ($s = 1.5$).

is in the range $\alpha_{\max} < \delta\alpha < 2\alpha_{\max}$. This happens when one ray passes at $\sim \theta_s$ and the another ray passes at the opposite side of the lens in the direction connecting the lens center and the first ray. While if $\theta_{12} < \theta_s$, the largest excursion angle is smaller than α_{\max} . An important consequence of this is that for ray pairs with the separation angle larger than θ_s , the maximum excursion angle does not strongly depend on the ray separation but lies in a small range of $(1-2)\alpha_{\max}$, and it scales with the halo mass as $\propto M^{2/3}$.

3.3 PDF of $\delta\alpha$

Let us first consider the probability distribution induced by one halo, which we denote by $\text{PDF}_1(\delta\alpha|\theta_{12})$. Let $p(\theta)$ be the probability of a ray passing at a small area $\theta \rightarrow \theta + \delta\theta$ from a lens center, which is given by the cross section area (denoted by A) normalized by the unit solid angle ($d\Omega$):

$$p(\theta) = \frac{A(\theta \rightarrow \theta + \delta\theta)}{d\Omega}. \quad (18)$$

Then $\text{PDF}_1(\delta\alpha|\theta_{12})$ is given by the joint probability,

$$\text{PDF}_1(\delta\alpha|\theta_{12}) = \int \frac{d^2\theta_1}{d\Omega} \int \frac{d\phi_{12}}{2\pi} p(\theta_1) p(\theta_1 + \theta_{12}), \quad (19)$$

where $\theta_{12} = \{\theta_{12} \cos(\phi_{12}), \theta_{12} \sin(\phi_{12})\}$. Note that since we are considering lensing by a single halo having a certain density profile and mass, given a configuration of a light ray pair, its excursion angle is *uniquely determined*. The total $\text{PDF}(\delta\alpha|\theta_{12})$ is obtained by summing $\text{PDF}_1(\delta\alpha|\theta_{12})$ over halos within a light-cone volume,

$$\begin{aligned} \text{PDF}(\delta\alpha|\theta_{12}) &= \int dV \int dM n_{\text{halo}}(M, z) \text{PDF}_1(\delta\alpha|\theta_{12}) \\ &= \int_0^{r(z_s)} dr r^2 \int dM \\ &\quad \times n_{\text{halo}}(M, r[z]) \text{PDF}_1(\delta\alpha|\theta_{12}), \end{aligned} \quad (20)$$

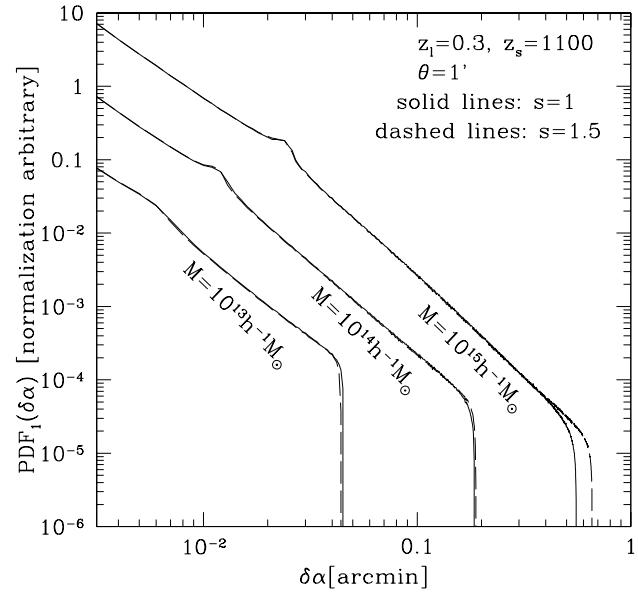


Figure 8. PDF of the lensing excursion angles from one halo, $\text{PDF}_1(\delta\alpha)$, for three halo masses $M_{\text{halo}} = 10^{13}, 10^{14}$ and $10^{15} h^{-1} M_{\odot}$. The normalization is arbitrary. The lens and source redshifts are $z_l = 0.3$ and $z_s = 1100$, respectively. The solid lines are for $s = 1$ and dashed lines are for $s = 1.5$. The concentration parameter taken is $c_* = 8$ for all cases.

where r is the comoving radial distance, $dV = r^2 dr$ (this expression is valid only for a flat cosmological model) is the unit volume element and $n_{\text{halo}}(M, z)$ is the halo mass function. We adopted the mass function by Sheth & Tormen (1999). Note that this approach breaks down for small excursion angles where secular scattering by distant and/or small halos are important, which generate the Gaussian core of the excursion-angle distribution.

3.4 Results

Let us start with the excursion angle PDFs from one halo plotted in Figure 8 which help to understand the origin of the exponential tail. The most important point which should be noticed is the sharp cut-off in a large excursion angle. This is a natural consequence of the fact that the deflection angle of the universal density profile halo is finite (see §3.1). The maximum excursion angle scales with the halo mass roughly as $\propto M^{2/3}$ (with a small correction by the mass dependence of the concentration parameter) as far as the separation angle is larger than the angular scale radius (θ_s) of a lensing halo, as explained in the last subsection. The other important point is that the mass-independent double power-law slope, its power-law slope is $\propto \delta\alpha^{-2}$ for smaller excursion angles and $\propto \delta\alpha^{-2.64}$ for larger angles. The former is generated by ray pairs in which both rays pass outside of the virial radius, while the latter is generated by pairs of rays of which one passes outside of the halo, and the other inside.

Under the assumptions stated in the last subsection, the excursion angle PDF is obtained by summing up contributions from single halos over a wide range of the halo mass and integrating over the redshift of halos as defined by eq. (20). We plot the PDF computed from such a model

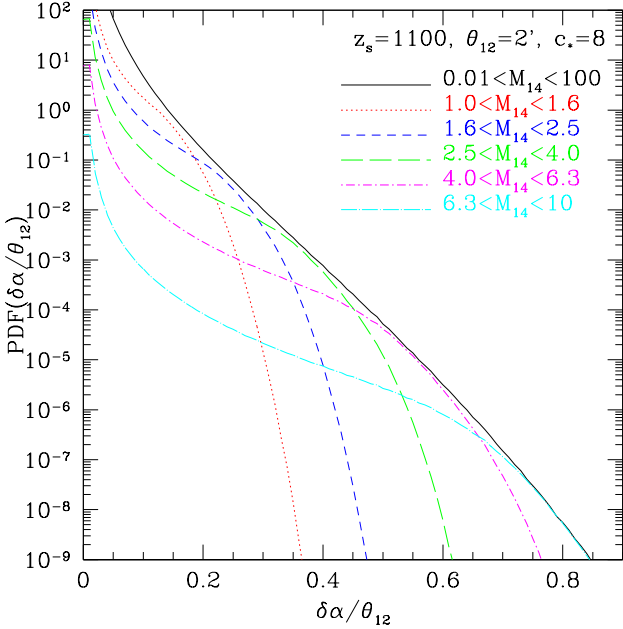


Figure 9. Model prediction of the lensing excursion angle PDF for $z_s = 1100$, $c_* = 8$ and $s = 1$. The black line shows the full PDF, while the colored lines show contribution from a limited range of the halo mass denoted in the panel.

in Figure 9. The black line shows the total PDF, while colored lines represent contributions from narrow limited mass ranges. This Figure clearly illustrates the origin of the exponential tail. There are two key points; a large excursion angle can only be generated by massive halos with mass typically larger than $10^{14} h^{-1} M_\odot$, and at such a halo mass range, the mass function decreases exponentially. Accordingly, the number of more massive halos that can contribute to a larger excursion angle decreases exponentially, and as a result, the exponential slope of the PDF arises.

In order to examine what redshift range of halos makes a major contribution to the exponential tail, we plot in Figure 10 the excursion angle PDFs computed for limited ranges of the lens redshifts (upper panel) and their percentage of the contribution (lower panel). It is seen in the lower panel that contributions from halos at redshifts below 1 account for almost full amplitude of the PDF tail. This is explained by a rapid evolution of the halo mass function at the high mass end. In fact, the number density of massive halos with $M_{\text{halo}} \gtrsim 2 \times 10^{14} h^{-1} M_\odot$ decreases by more than one order of magnitude from $z = 0$ to 1.

The above results lead to the following explanation for the origin of the lensing excursion-angle PDF which has two components, a Gaussian core and an exponential tail: The light rays emitted at high redshifts undergo many gravitational deflections by (large- or small-scale) structures on their way to us, which after many uncorrelated deflections produces the Gaussian core. Some small part of the rays is strongly lensed by a massive halo with mass larger than $10^{14} h^{-1} M_\odot$ at a low redshift of $z < 1$, and the coherent deflections caused by the strong lensing produce the exponential tail. Therefore even if a ray pair encounters a strong coherent deflection by a single massive halo, its excursion angle is not solely determined by the strong halo lensing

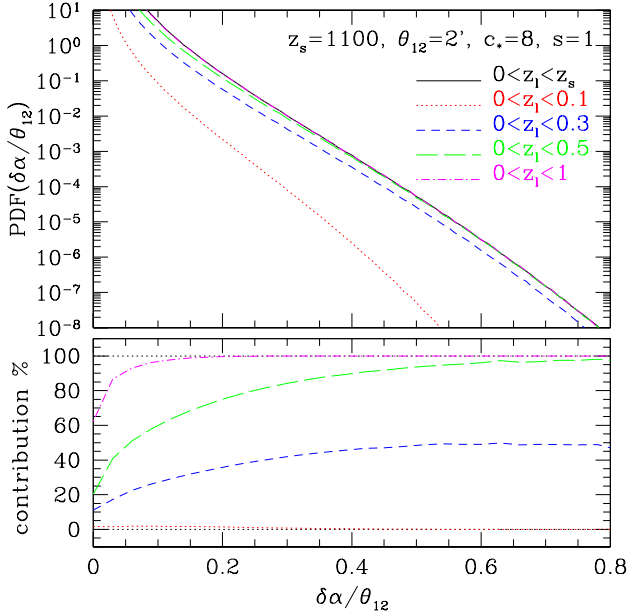


Figure 10. Model prediction of the lensing excursion angle PDF for $z_s = 1100$, $c_* = 8$ and $s = 1$. The black line shows the full PDF, while the colored lines show contribution from a limited range of the lens redshift denoted in the panel.

but the random scattering also contributes to it to a smaller extent. This effect on the PDF is taken into account by the convolution:

$$E(x) = \int dy G(y) E'(x - y), \quad (21)$$

where $G(y)$ denotes the Gaussian distribution, and $E'(x)$ denotes the tail part produced by the halo lensing without considering the contribution from the random scattering (which could be computed by the model described in this section). Since, as shown in Figure 9, the tail is well approximated by the exponential shape with a constant index over a wide range of $\delta\alpha$, it is reasonable to approximate $E'(x) \simeq p' \exp(-qx)$ and,

$$\begin{aligned} E(x) &\simeq \frac{p'}{\sqrt{2\pi}\sigma} \int dy \exp\left(-\frac{y^2}{2\sigma^2}\right) \exp(-q(x - y)) \\ &= p \exp(-qx), \end{aligned} \quad (22)$$

with the boosted amplitude,

$$p = p' \exp\left(\frac{(\sigma q)^2}{2}\right). \quad (23)$$

Thus under the above approximation, the slope of the exponential tail is unchanged but the amplitude is increased. This combined with the fact that almost all contributions to the PDF tail come from coherent scattering by massive halos at $z < 1$ (Figure 10) accounts for the trend observed in the excursion angle PDFs obtained from the ray-tracing simulation that its slope does not depend strongly on the source redshift but its amplitude increases with the source redshift. Actually, a very similar trend is observed in the model PDFs plotted in Figure 11 which shows the corrected PDF tails for $z_s = 1, 3$ and 1100 and for four ray separations. Here, in order to compute the boost factor of eq. (23), we

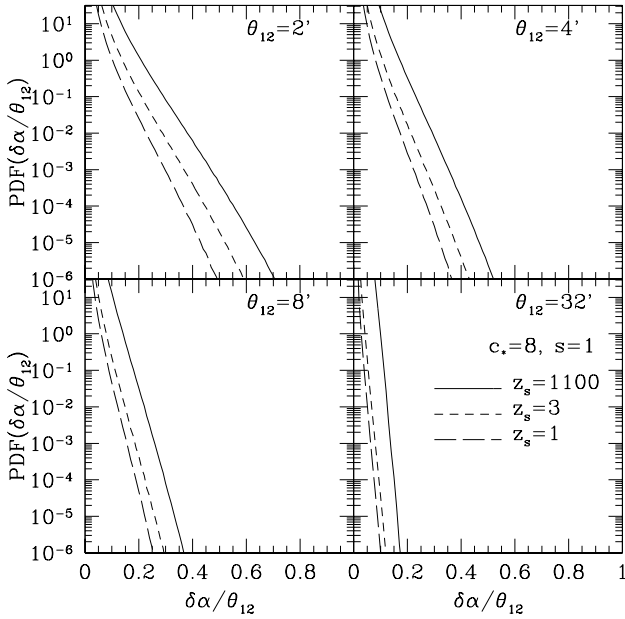


Figure 11. The model predictions of the lensing excursion angle PDF after the correction to the accumulative lensing effect being made (using the approximate way of eq. (22)). The halo parameters are $c_* = 8$ and $s = 1$. The ray separations are denoted in each plot. The source redshifts are, from inner to outer, $z_s = 1, 3$ and 1100, respectively.

compute p' and q by fitting the model PDFs at two points, $\text{PDF}(x_1) = 1.0 \times 10^{-2}$ and $\text{PDF}(x_2) = 1.0 \times 10^{-3}$ to the exponential function. Note that after this correction the amplitude of the tails can be increased more than one order of magnitude because of the steep slope of the exponential tail (thus for a large q).

Four panels of Figure 12 show the corrected model PDFs for various values of c_* and s , which help to understand the dependences of the shape of the PDF tail on the halo parameters. Clearly, the broader tail appears for models with a larger c_* or a larger s , because such models generate a larger maximum deflection angle. It is important to notice that a small change of c_* or s causes a very large, nonlinear change in the shape and amplitude of the PDF. Therefore, choosing mean values of c_* and s does not provide a mean PDF but gives a lower amplitude. It should be noted that the halo model parameters indeed have a large scatter (Jing 2000; Jing & Suto 2000; see also Figure 9 of Hamana et al. (2004) which clearly shows that the compactness of halo mass distributions has a large scatter).

Finally, we compare in Figure 13 the parameters in the exponential function eq. (22) measured from the model PDFs (symbols with lines), with the results from the ray-tracing experiments. We evaluate p and q by fitting the corrected model PDF (i.e., after the correction by eq. (22) being made). As shown in Figure 13, the parameter q correlates with the slope parameter q as expected. The measured exponential slope parameter q plotted in the lower panel are larger than the results from the numerical experiments, though the slope with the separation angle is very similar. The discrepancy is smaller for models with a larger c_* or a larger s . Therefore the model prediction may be improved

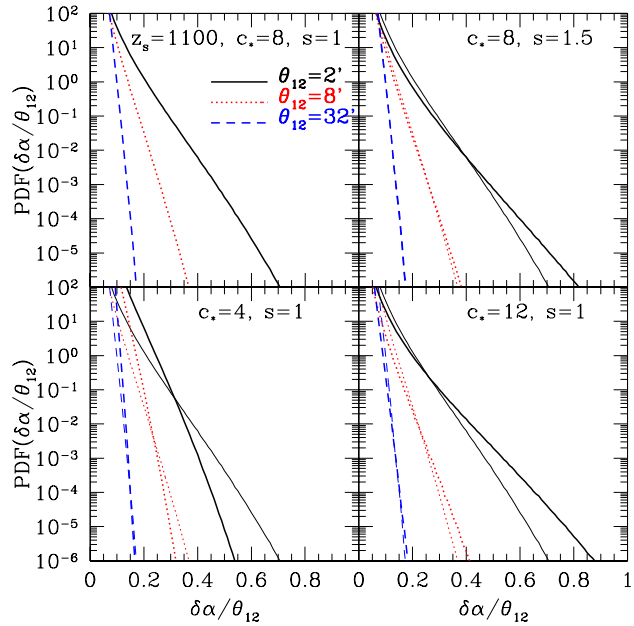


Figure 12. The model predictions of the lensing excursion angle PDFs. We have applied the corrections given by equations (22) and (23). Ray separations are $\theta = 2, 8$ and 32 arcmin (solid, dotted and dashed, respectively). The source redshift is taken by $z_s = 1100$. Halo model parameters are denoted in each panel. The thin lines in the top right and two bottom panels show, for comparison, the predictions of the fiducial model plotted in the top left panel.

if one takes into account the scatter in the halo parameters c_* or a larger s .

Quantitatively, none of the four models plotted in Figures 12 and 13 are in very good agreement with the simulation results. The discrepancy is partly due to the scatter in the halo model parameters as has been discussed above. Also, a deviation in the halo mass distribution from spherical symmetry could partly account for it. Actually, the mass distribution of most of the halos significantly deviates from spherical symmetry (Hamana et al. 2004). In addition, the spatial correlation of halos may have an influence on the excursion angle PDF, because massive halos are strongly clustered. A close look at the sky distributions of ray pairs having a large excursions angle and of massive halos shown in Figure 6 reveals that those deviations from our simple model should indeed play a role; namely, it is seen in the Figure that a small part of most massive halos does not produce a large lensing excursion event, and that a small part of large excursion angle ray pairs does not intersect a very massive halo.

We may conclude, from what has been seen above, that our simple model succeeds in getting the essential mechanism of generating the exponential tail and in explaining the origin of the major characteristics of the tail. The model predictions are in reasonable agreement with the simulation results. Further modifications of the model taking into account details of halo properties, such as scatter in the halo model parameters, deviations of the halo mass distribution from spherical symmetry and clustering of halos, are needed to improve the accuracy of the model prediction..

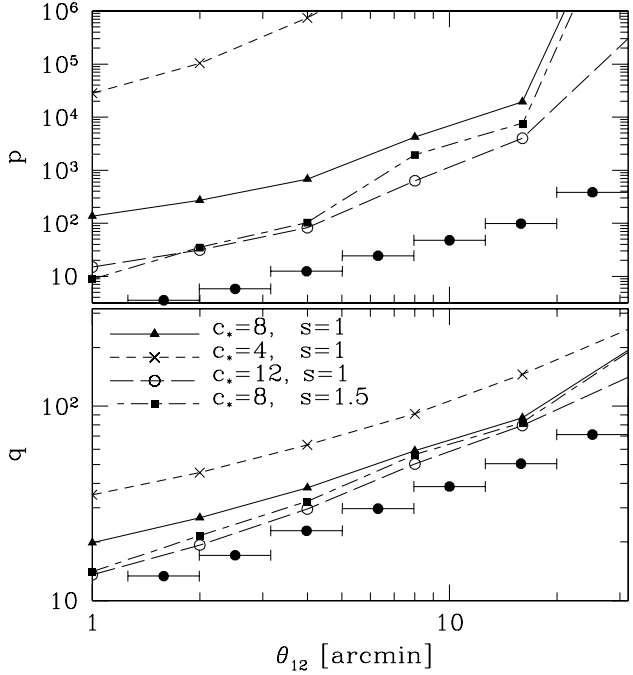


Figure 13. Parameters in the exponential distribution (eq. 22) computed from the fit to the model predictions of excursion angle PDFs for $z_s = 1100$. Model parameters are denoted in the plot. Dotted lines show the results from ray-tracing simulation.

4 SUMMARY AND DISCUSSIONS

We have investigated the statistical distribution of lensing excursion angles, paying a special attention to the physical processes that are responsible for generating two components of the PDFs: the Gaussian core and the exponential tail. We have used the numerical gravitational lensing experiments in a CDM cosmology to quantify these two components.

The origin of the Gaussian core is explained by the random lensing deflections by either linear or nonlinear structures. The variances of the Gaussian core measured from the results of the numerical experiments are found to be in a good agreement with the prediction by the power spectrum approach (Seljak 1994; 1996).

The presence of the exponential tail was first found by Hamana & Mellier (2001) but its origin remains unrevealed. The tail is characterized by two parameters: the slope and amplitude. We have found from the numerical experiments that the slope changes little with the source redshift while the amplitude becomes greater as the source redshift increases, at least within the redshift range we consider ($1 < z_s < 1100$). Since the random lensing deflections result in the Gaussian core, the exponential tail is most likely to result from coherent deflections. In addition, in order to generate a large excursion angle, massive virialized objects should be responsible for the exponential tail. Therefore, we supposed that the exponential tail originates from coherent lensing scatters by single massive halos.

We have developed a simple empirical model for the exponential tail of the lensing excursion angles PDF. We used the analytic models of the dark matter halos, namely the modified Press-Schechter (Press & Schechter 1974) mass

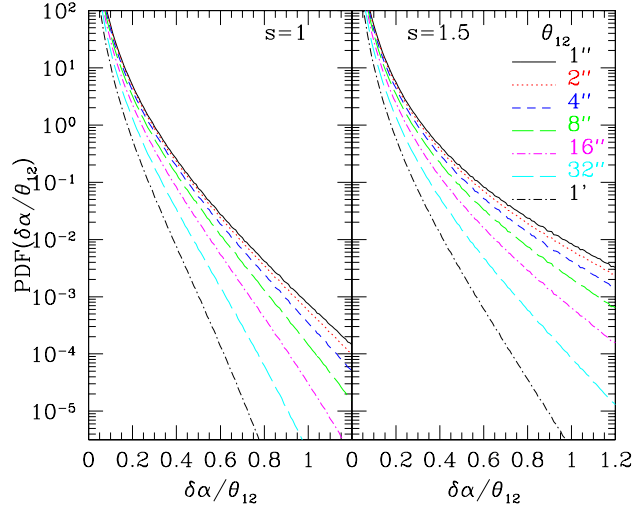


Figure 14. The empirical model predictions of the tail part of the excursion angle PDF for sub-arcmin ray separations. The source redshift is $z_s = 1100$, the concentration parameter is $c_* = 8$ and the inner slope is $s = 1$ (left) and $s = 1.5$ (right).

function (Sheth & Tormen 1999) and the Universal density profile first proposed by Navarro et al. (1996). Although we only consider a coherent lensing scatter by a single massive halo and did not take into account the scatters in the halo parameters (the concentration parameter c_* and the inner slope s), our model reasonably reproduces the exponential tails computed from the numerical experiments. It is found that the massive halos with $M > 10^{14} h^{-1} M_\odot$ are responsible to the tail and that the exponential shape arises as a consequence of the exponential cutoff of the halo mass function at such mass range. Almost all contributions to the tail come from the halos at redshifts below 1. Therefore, the slope of the tail is formed by the halos at $z < 1$. On the other hand, the amplitude of the tail is determined by the convolution of two contributions, the coherent scatter and the random deflections. Since the contribution from the random deflections becomes greater as the source redshift increases, the amplitude of the tail becomes greater for a higher source redshift. These explain the redshift-independent slope and the redshift-dependent amplitude found from the numerical experiments.

Does the exponential tail have an influence on the angular power spectrum of the temperature map of the cosmic microwave background (C_ℓ)? As far as angular scales larger than 1 arcmin are concerned, the answer is no. When one computes the lensed C_ℓ one can safely use the approximate convolution equation given by Seljak (1996), because the key assumption in the approximation made for deriving the convolution equation is not the Gaussianity of the excursion angle PDF, but that its variance is small (cf. §9 of Bartelmann & Schneider 2001). Since the smallness of the variance is also the case for lower redshifts, the same convolution technique can be applied to other angular correlation functions such as that of galaxies and QSOs.

Before closing this paper, we present predictions for tails of the excursion angle PDF for sub-arcmin ray separations. We plot in Figure 14 our empirical model predictions. It is found that for ray separations $\theta_{12} > 10$ arcsec, the ampli-

tude of the tail keeps increasing with the slope becoming flatter in a similar rate of larger separations. However below that separation, the growth rate becomes smaller gradually. The standard dispersions of these distributions are smaller than unity but can be of order $O(0.1)$ which is comparable to that of the Gaussian core, though our simple model adopting average halo parameters tends to predict greater amplitude than the results from the numerical experiments (see §3.4). Therefore, it is possible that on arcsecond scales coherent lensing deflections have non-negligible influence on the angular clustering of objects in the distant universe. Note that even if taking the exponential tail into account, the standard dispersion of the excursion angles is less than unity, thus the approximate convolution equation can be still valid but the contribution from the tail to the dispersion should be included. We notice that it is however not clear whether the assumptions in our model are still valid on such small ray separations. The statistical distribution of lensing excursion angles for arcsecond separation ray pairs should be investigated in a future work with a gravitational numerical experiment having a higher resolution.

ACKNOWLEDGMENTS

The N -body simulations used in this work were carried out by the Virgo Consortium at the computer center at Max-Planck-Institut, Garching (<http://www.mpa-garching.mpg.de/NumCos>). Numerical computations presented in this paper were partly carried out at ADAC (the Astronomical Data Analysis Center) of the National Astronomical Observatory Japan, at the Yukawa Institute Computer Facility and at the computing center of the Max-Planck Society in Garching.

REFERENCES

Bartelmann, M., 1996, A&A, 313, 697
 Bartelmann M., Schneider P., 1992, A&A, 259, 413
 Bartelmann M., Schneider P., 2001, Physics Report, 340, 291
 Bullock J. S., Kolatt T. S., Sigad Y., Somerville R. S., Kravtsov A. V., Klypin A. A., Primack J. R., Dekel A., 2001, MNRAS, 321, 559
 Fukushige T., Makino J., 2001, ApJ, 557, 533
 Fukushige T., Makino J., 2003, ApJ, 588, 674
 Ghigna S., Moore B., Governato F., Lake G., Quinn T., Stadel J., 2000, ApJ, 544, 616
 Hamana, T., Martel, H., Futamase, T. 2000, ApJ 529, 56
 Hamana, T., Mellier, Y. 2001, MNRAS, 169, 176
 Hamana, T., Takada, M., Yoshida, N., 2004, MNRAS, 2004, 350, 893
 Hamana T., Yoshida N., Suto Y., 2002, ApJ, 568, 455
 Henry, J. P., 2000, ApJ, 534, 565
 Hockney, R. W., Eastwood, J. W., 1988, Computer Simulation Using Particles (Adam Hilger, Bristol)
 Jain, B., Seljak, U., 1997, ApJ, 484, 560
 Jain, B., Seljak, U., White, S. D. M., 2000, ApJ, 530, 547
 Jenkins A., Frenk C.S., White S.D.M., Colberg J.M., Cole S., Evrard A.E., Couchman H.M.P., Yoshida N., 2001, MNRAS, 321, 372
 Jing, Y. P., 2000, ApJ, 535, 30
 Jing Y. P., Suto Y., 2000, ApJ, 529, L69
 Keeton C. R., Madau P., 2001, ApJ, 549, L25
 Macfarland, T., Couchman, H. M. P., Pearce, F. R., Pichlmeier, J., 1998, New Astronomy, 3, 687
 Ménard, B., Hamana, T., Bartelmann, M., Yoshida, N., 2003, A&A, 403, 817
 Moore B., Governato F., Quinn T., Statal J., Lake G., 1998, ApJ, 499, L5
 Moore B., Quinn T., Governato F., Statal J., Lake G. 1999, MNRAS, 310, 1147
 Nakamura, T. T., & Suto, Y. 1997, Prog. Theor. Phys., 97, 49
 Navarro J., Frenk C., White S. D. M., 1996, ApJ, 462, 564
 Navarro J., Frenk C., White S. D. M., 1997, ApJ, 490, 493
 Oguri M., Taruya A., Suto Y., 2001, ApJ, 559, 572
 Peacock J.A., Dodds S.J., 1996, MNRAS, 280, L19
 Press W. H., Schechter P., 1974, ApJ, 187, 425
 Schneider P., Ehlers J., Falco, C. C., 1992, Gravitational Lenses, Springer-Verlag, New York
 Seljak U., Zaldarriaga M., 1996, ApJ, 469, 437
 Seljak U., 1994, ApJ, 436, 509
 Seljak U., 1996, ApJ, 463, 1
 Sheth R. K., Tormen G., 1999, MNRAS, 308, 119
 Takada M., Jain B., 2003, MNRAS, 340, 580
 Vale, C., White, M., 2003, ApJ, 592, 699
 White, S. D. M. 1996, in Cosmology and Large-Scale Structure, ed. R. Schaefer, J. Silk, M. Spiro, & J. Zinn-Justin (Dordrecht: Elsevier)
 Wright, C. O., Brainerd, T. G., 2000, ApJ, 534, 34
 Yoshida N., Sheth R. K., Diaferio A., 2001, MNRAS, 328, 669